

We are IntechOpen, the world's leading publisher of Open Access books Built by scientists, for scientists

6,900

Open access books available

186,000

International authors and editors

200M

Downloads

Our authors are among the

154

Countries delivered to

TOP 1%

most cited scientists

12.2%

Contributors from top 500 universities



WEB OF SCIENCE™

Selection of our books indexed in the Book Citation Index
in Web of Science™ Core Collection (BKCI)

Interested in publishing with us?
Contact book.department@intechopen.com

Numbers displayed above are based on latest data collected.
For more information visit www.intechopen.com



Wavelet Transforms in Dynamic Atomic Force Spectroscopy

Giovanna Malegori and Gabriele Ferrini

*Interdisciplinary Laboratories for Advanced Materials Physics (i-LAMP) and
Dipartimento di Matematica e Fisica, Università Cattolica del Sacro Cuore, I-25121 Brescia
Italy*

1. Introduction

Since their invention scanning tunneling microscopy (STM, (Binnig et al., 1982)) and atomic force microscopy (AFM, (Binnig et al., 1986)) have emerged as powerful and versatile techniques for atomic and nanometer-scale imaging. In this review we will focus on AFM, whose methods have found applications for imaging, metrology and manipulation at the nanometer level of a wide variety of surfaces, including biological ones (Braga & Ricci, 2004; Garcia, 2010; Jandt, 2001; Jena & Hörber, 2002; Kopniczky, 2003; Morita et al., 2009; 2002; Yacoot & Koenders, 2008). Today AFM is regarded as an essential tool for nanotechnology and a basic tool for material science in general.

AFM relies on detecting the interaction force between the sample surface and the apex of a sharp tip protruding from a cantilever, measuring the cantilever elastic deformation (usually its bending or twisting) caused by the interaction forces. Fig. 1a shows a schematic interaction force dependence on tip-sample distance in vacuum (Hölscher et al., 1999). As the distance between the cantilever and the sample surface is reduced by means of a piezoelectric actuator, the tip first experiences an attractive (typically van der Waals) force, that increases to a maximum value. During further approach, the attractive force is reduced until a repulsive force regime is reached. Therefore the AFM is a sensitive force gauge on the nanometer and atomic scale (Butt et al., 2005; Cappella & Dietler, 1999; Garcia & Perez, 2002; Giessibl, 2003; Mironov, 2004).

The use of AFM in such tip-sample force measurements is commonly referred to as *force spectroscopy*. The simplest technique used for quantitative force measurements involves directly monitoring the static deflection of the cantilever as the tip moves towards the surface (approach curve) and then away (retraction curve), providing a deflection versus distance plot. To obtain a force-distance curve, the cantilever deflection is converted to tip-sample interaction force using Hooke's law (Butt et al., 2005; Cappella & Dietler, 1999), after calibration of the cantilever spring constant (Hutter & Bechhoefer, 1993; Sader, 1999).

A typical force curve at room temperature and in air is shown in Fig. 1b (Butt et al., 2005; Cappella & Dietler, 1999). During the approach to the surface, an attractive long-range force on the probe bends the cantilever toward the surface. Then the tip suddenly jumps into contact with the surface due to the large gradient of the attractive force near the sample surface

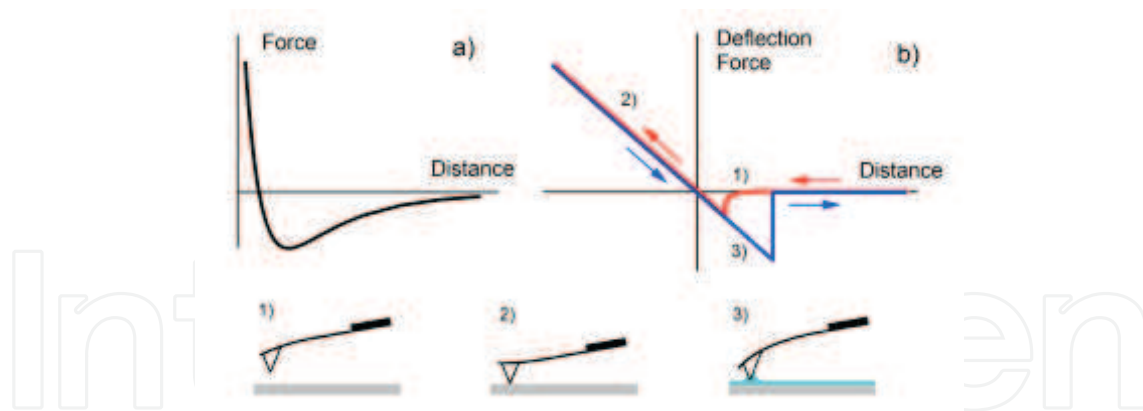


Fig. 1. a) Schematic diagram of the tip-sample forces as a function of distance in vacuum. b) Schematic picture of a typical force curve in air, showing the cantilever deflection (proportional to the applied force) versus the tip-sample distance during approach (red) and withdrawing (blue). The cantilever interactions in the various zones of the force curve are illustrated below: 1) attractive long-range interaction, 2) repulsive contact interaction, 3) adhesive capillary force.

(van der Waals, adhesion, capillary forces, electrical interactions). A further approach of the cantilever to the sample leads to an increasing cantilever deflection in the opposite direction due to repulsive contact force. Finally, during the retraction curve, the tip-sample separation (jump-off contact) occurs at distance larger than the jump to contact distance. The hysteresis is usually due to adhesive capillary force which keeps the tip in contact to the sample.

Depending on their compliance, the cantilever, tip and sample may experience an elastic or plastic deformation. In case of elastic interaction, the linear parts of the force-distance curve recorded during forward and reverse motion coincide. For compliant samples, such as biological samples, the shape of the curves is more complex due to indentation effects. Generally, the force-distance curve provides information on the nanoscale tip-surface interactions, the local elasticity of the sample and the adhesion forces (Andreeva et al., 2010; Butt et al., 2005; Cappella & Dietler, 1999; Radmacher et al., 1996).

More refined techniques, suitable for atomic scale investigations in vacuum and in liquids, rely on measuring the dynamic parameters of the cantilever excited at or near its resonant frequency while experiencing the force field of the sample surface. The interactions of the tip with the sample surface perturbs the amplitude, frequency, phase or damping of the cantilever oscillation. The tip-sample interaction force can be inferred by the modifications of these parameters (Albrecht et al., 1991; Crittenden et al., 2005; Hölscher et al., 1999; Lantz et al., 2001; Martin et al., 1987; Palacios-Lidón & Colchero, 2006; Sugimoto, Innami, Abe, Custance & Morita, 2007).

There are two basic methods in dynamic AFM operations, the Amplitude Modulation (AM) technique (Martin et al., 1987) and the Frequency Modulation (FM) technique (Albrecht et al., 1991).

AM-AFM detect the variation of amplitude and phase of the excited cantilever oscillations due to tip-sample interactions and has been successfully implemented in ambient conditions involving repulsive tip-sample interactions, the so called "tapping mode". Though extremely

interesting, these techniques will not be considered further in this review and the interested reader is referred to the bibliography (Garcia, 2010; Garcia & Perez, 2002).

FM-AFM detects with high sensitivity minute changes in the cantilever resonant frequency under a particular feedback mode, while the tip approaches the surface (Giessibl, 2003; Morita et al., 2009; 2002). The tip-sample force versus distance can be inferred by inverting the resonance frequency shift versus distance curves (Giessibl, 2003; Hölscher et al., 1999; Sader & Jarvis, 2004). This technique detects long-range electrostatic and van der Waals forces as well as repulsive short-range force providing the chemical identification of single atoms at surfaces. In fact, short-range interaction depends primarily on the chemical identity of the atoms involved since they are associated with the onset of the chemical bond between the outermost atom of the tip apex and the surface atoms. Then precise measurement of such short-range chemical force allows to distinguish between different atomic species even though they exhibit very similar chemical properties and identical surface position preferences so that any discrimination attempt based on topographic measurements is impossible (Gross et al., 2009; Lantz et al., 2001; Sugimoto, Pou, Abe, Jelinek, Pérez, Morita & Custance, 2007). Moreover, FM-AFM has recently attained atomic scale resolution in liquids, (Fukuma, 2010; Fukuma et al., 2010).

Three dimensional frequency shift maps over a surface have been acquired too, a method known as 3D AFM spectroscopy. Measuring the frequency shift and the topography over finely spaced planes parallel to the sample surface, allows to apply drift corrections to the data and retrieve a three dimensional frequency shift grid. From these data, the interaction forces, by inverting each frequency-shift versus distance curve, the tip-sample potential energy and the energy dissipated per oscillatory cycle are obtained (Albers et al., 2009).

An interesting alternative to performing force spectroscopy is the broad band excitation (BE) scheme which takes advantage of the fact that the simultaneous analysis at all frequencies within the excited band reduces the acquisition time. Broad band excitation can be achieved by an external driving force (Jesse et al., 2007) or by thermal excitation (Malegori & Ferrini, 2010a; Roters & Johannsmann, 1996; Vairac et al., 2003).

In the first case, instead of a simple sinusoidal excitation, the BE method uses a driving signal with a predefined spectral content in the frequency band of interest. The cantilever response to the BE drive is measured and Fourier transformed to yield the amplitude and phase-frequency curves at several distances from the surface. The measured response curves allow to calculate the resonant frequency, amplitude, and Q-factor at each distance and display the data as a 2D image. Again, the force versus distance curve can be inferred from the evolution of the frequency, the energy dissipation from the phase and quality factor modifications. The fast Fourier transform/fitting routine replaces the traditional lock-in/low pass filter that provides amplitude and phase at a single frequency at time. In the BE method the system is excited and the response is measured simultaneously at all frequencies within the excited band (parallel excitation/detection). On the contrary, standard lock-in detectors acquire the response over a broad band by sampling one frequency at time. In both cases the complete spectral acquisition is carried out at several tip-sample separation. The BE approach allows a significant reduction of the acquisition time by performing the detection on all frequencies in parallel, so that an extremely broad frequency range (25-250 kHz) can be probed in ~ 1 s. A comparable scan over the same frequency band using a lock-in would require ~ 30 min.

Another possibility in broad band excitation is the *thermal excitation*, essentially a random force of thermal origin due to the interaction of the cantilever with the surrounding environment (the thermal reservoir). The random force power spectrum does not depend on frequency and produces the so called Brownian motion or white noise (Callen & Greene, 1952). A fundamental point is that the Brownian motion of the thermally driven cantilever is modified by the tip-sample interaction forces. It follows that the temporal trace of the cantilever thermal fluctuation detected at various distances from the surface contains informations on the tip-sample interaction and can be analyzed to reconstruct the tip-sample potential and interaction force.

Three different approaches are possible: (a) to measure the shift of the cantilever resonant frequency of the first flexural modes as the tip moves toward the surface to retrieve the gradient of the interaction forces (Roters & Johannsmann, 1996); (b) to detect the mean square displacement of the tip subjected to thermal motion in order to estimate the interaction force gradient dependence on the tip-sample distance (Malegori & Ferrini, 2010a); (c) to analyze the probability distribution of the tip's position during the Brownian motion. Then the Boltzmann distribution is used to calculate the Helmholtz free energy of the tip interacting with the surface as a function of the tip-sample distance. The interaction force gradient is inferred from the second derivative of the Helmholtz free energy (Cleveland et al., 1995; Heinz et al., 2000; Koralek et al., 2000). In (Malegori & Ferrini, 2010a) the three methods have been applied simultaneously to the same experimental session to compare their peculiarities.

BE methods provides the lower limits on the acquisition time required to detect a complete force versus distance curve (0.1-1 s). Nevertheless, this acquisition time is still too long and incompatible with the rate of 1-30 ms/pixel which is the value necessary to obtain a complete force image. This motivated the introduction of the wavelet transform in thermally excited dynamic spectroscopy, a new approach to spectroscopy measurements that is the topic of this review. Wavelet transforms allow to reduce the acquisition time to values compatible with practical dynamic force spectroscopy imaging and to apply the analysis simultaneously to all the cantilever modes, either flexural and torsional, within the cut-off frequency of the acquisition system.

2. Thermally excited cantilever: the Brownian motion

2.1 Fluctuation-dissipation theorem

At non zero absolute temperature, a system in thermodynamic equilibrium is not at rest but continuously fluctuates around its equilibrium state. For example, a mechanical system in equilibrium at temperature T , continuously exchanges its mechanical energy with the thermal energy of the thermal bath in which it is immersed.

To analyze the thermal fluctuations of a system, consider an extensive variable x which is coupled to the intensive parameter F in the Hamiltonian of the system (Callen & Greene, 1952; Paolino & Bellon, 2009). In the frequency domain, the response function $G(\omega)$ describes the response of the system to the driving variable F . It is defined as:

$$G(\omega) = \frac{F(\omega)}{x(\omega)}$$

The thermal fluctuations of the observable x are described by the Fluctuation-Dissipation theorem (Gillespie, 1993; 1996) which connects the power spectral density (PSD) of the fluctuations of the variable x , $S_x(\omega)$, to the temperature and the response function $G(\omega)$ as:

$$S_x(\omega) = \frac{x^2(\omega)}{\Delta\omega} = -\frac{2k_B T}{\omega} \Im \left[\frac{1}{G(\omega)} \right] \quad (1)$$

Here k_B , $\Delta\omega$ and $\omega = 2\pi f$ are the Boltzmann constant, the angular frequency bandwidth and the angular frequency or pulsation associated to frequency f and \Im denotes the imaginary part. The average shape of a spontaneous fluctuation is identical with the observed shape of a macroscopic irreversible decay toward equilibrium and is, therefore, describable in terms of the macroscopic response function.

2.2 Dynamic response of the cantilever

An example of mechanical dissipative system is the AFM cantilever placed in air far from the surface (free cantilever) and driven by background thermal energy. The cantilever is in thermal equilibrium with the molecules of the fluid in which it is immersed. In this situation it fluctuates mainly in response to stochastic forces due to the molecular motion from the temperature of the thermal bath.

The cantilever is described as an elastic massless beam (with elastic constant k). One end is fixed to the chip whereas a mass m (the tip) is localized on the free end. Then the cantilever dynamics can be reasonably modeled as a stochastic harmonic oscillator with viscous dissipation (Gillespie, 1996; Paolino & Bellon, 2009; Shusteff et al., 2006). In this case x is the displacement from equilibrium of the tip and F is the force applied to the system. For a non-interacting cantilever, the external driving force F is the thermal stochastic force F_{th} , which accounts for the interaction with the local environment. The resulting Brownian motion of the tip displacement x is described by the second order Langevin equation

$$m\ddot{x}(t) + \gamma\dot{x}(t) + kx(t) = F_{th}(t) \quad (2)$$

where γ is the damping factor.

F_{th} is defined by its statistic properties (Langevin hypothesis (Gillespie, 1993; 1996)) as a zero-mean force ($\langle F_{th}(t) \rangle = 0$), completely uncorrelated in time

$$\langle F_{th}(t)F_{th}(t + \tau) \rangle = \alpha\delta(\tau) \quad (3)$$

Here the brackets $\langle \rangle$ denote time averaging, $\delta(\tau)$ is the Dirac delta function and α a proportionality constant which will be determined through the fluctuation-dissipation theorem.

The Wiener-Khinchine theorem (Callen & Greene, 1952; Gillespie, 1996) states that, for a stationary random process, the power spectral density and its temporal autocorrelation function are mutual Fourier transforms. Applying the theorem to the the power spectrum of the thermal activating force $S_F(\omega)$ we obtain

$$S_F(\omega) = \hat{A}_F(\omega) = \alpha \quad (4)$$

where $\hat{A}_F(\omega)$ is the Fourier transform of the autocorrelation function $A_F(\tau) = \langle F_{th}(t)F_{th}(t + \tau) \rangle$. The stochastic force of the physical system is called *white noise* because it has no frequency dependence.

Now it is possible to connect the correlation function, that characterizes the fluctuating forces, to the dissipative part of the equation of motion, i.e. the damping factor γ .

The transfer function of the system is provided by writing Eq. 2 in Fourier space (frequency domain) as

$$G(\omega) = k \left[1 - \frac{\omega^2}{\omega_0^2} + i \frac{\omega}{Q\omega_0} \right] \quad (5)$$

where we introduced the resonant angular pulsation $\omega_0 = \sqrt{k/m}$ and the quality factor $Q = m\omega_0/\gamma$. The PSD of the thermal fluctuations x , using Eq. 1, is given by

$$S_x(\omega) = \frac{2k_B T}{k\omega_0} \frac{1/Q}{(1 - \omega^2/\omega_0^2)^2 + (\omega/\omega_0 Q)^2} \quad (6)$$

which is a Lorentzian curve with linewidth given by $\Delta\omega = \omega_0/Q$.

The PSD of the fluctuations $S_x(\omega)$ is related to the power spectrum of the stochastic thermal activating force $S_F(\omega)$ through the response function $G(\omega)$ (Shusteff et al., 2006) by $S_F(\omega) = S_x(\omega)G^2(\omega)$. Then from Eq. 5 and Eq. 6 we obtain

$$S_F(\omega) = 2k_B T \gamma \quad (7)$$

The constant α is determined by Eqs. 4 and 7 as $\alpha = 2k_B T \gamma$, providing an autocorrelation function of the external stochastic force expressed by:

$$\langle F_{th}(t)F_{th}(t + \tau) \rangle = 2k_B T \gamma \delta(\tau)$$

The last relation is another expression of the Fluctuation-Dissipation theorem which quantifies the intimate connection between the viscous coefficient γ and the randomly fluctuating force $F_{th}(t)$. It implies that the stochastic fluctuating force is an increasing function of γ and vanishes if and only if γ vanishes. The dissipative damping force $-\gamma\dot{x}$ and the fluctuating force F_{th} are correlated so that one cannot be present without the other one. This is because the microscopic events that give rise to those two forces simply cannot be separated into one kind of microscopic event (like the molecular collision) that gives rise *only* to a viscous effect and another kind that gives rise *only* to a fluctuating effect.

The Parseval relation is used to determine the variance of the fluctuations of the observable x (in our case the cantilever positional fluctuations) by integrating the positional PSD $S_x(\omega)$. Then:

$$\langle x^2 \rangle = \int_{-\infty}^{+\infty} S_x(\omega) d\omega = \frac{2k_B T}{k\omega_0 Q} \int_{-\infty}^{+\infty} \frac{d\omega}{\left(1 - \frac{\omega^2}{\omega_0^2}\right)^2 + \left(\frac{\omega}{Q\omega_0}\right)^2} = \frac{k_B T}{k} \quad (8)$$

The potential energy of the cantilever modeled as a damped harmonic oscillator takes the form of:

$$\frac{1}{2} m \omega_0^2 \langle x^2 \rangle = \frac{1}{2} k \langle x^2 \rangle = \frac{1}{2} k_B T$$

where $\langle x^2 \rangle$ represents the mean square displacement of the cantilever caused by the thermal motion in the direction normal to the surface. This relation is an expression of the equipartition theorem, stating that in a system in thermal equilibrium every independent quadratic term in its total energy has a mean value equal to $1/2k_B T$. An analysis of the cantilever thermal motion which explicitly considers all possible vibration modes can be found in (Butt & Jaschke, 1995).

Finally, we would like to point out that the reverse path is also possible, by demonstrating the Fluctuation-Dissipation theorem from the equipartition theorem, see (Gillespie, 1993; Shusteff et al., 2006).

2.3 Cantilever in interaction

Near the surface, the tip experiences an interaction force $F_{ts}(z)$, which depends on the distance $z = z(t)$ between the probe apex and the surface. The force is positive along the surface normal direction. The cantilever motion is now described by

$$m\ddot{x}(t) + \gamma\dot{x}(t) + kx(t) = F_{th}(t) + F_{ts}(z) \quad (9)$$

where x is the displacement from the equilibrium position of the free cantilever, see Fig. 2.

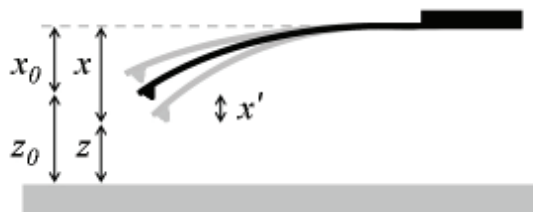


Fig. 2. Schematic representation of the variables describing the cantilever motion. z is the instantaneous tip-sample distance, positive along the surface normal direction. x is the instantaneous displacement from the equilibrium position of the free cantilever, negative when the cantilever is bent toward the sample. z_0 is the average tip-sample distance and x_0 the corresponding average tip displacement from the equilibrium under static interaction forces. $x' = x - x_0 = z - z_0$ is the cantilever displacement from the average equilibrium position under static interaction.

For small oscillations of x and z around the equilibrium position of the cantilever under static interaction, indicated as x_0 and z_0 , the derivative of the force can be considered constant for the whole range covered by the oscillating cantilever. Therefore the force may be approximated by the first (linear) term in the series expansion (Giessibl, 2003; Mironov, 2004):

$$F_{ts}(z) = F_{ts}(z_0) + \frac{\partial F_{ts}}{\partial z}(z_0)(z - z_0)$$

The constant term of the force $F_{ts}(z_0)$ statically deflects the cantilever in the new equilibrium position $x_0 = F_{ts}(z_0)/k$. The interaction force gradient influences the cantilever oscillations around this position. By introducing the displacement from the equilibrium position under static interaction $x' = x - x_0 = z - z_0$, which incorporates the cantilever static bending, (see

Fig. 2), we come to the equation

$$m\ddot{x}'(t) + \gamma\dot{x}'(t) + \left(k - \frac{\partial F_{ts}}{\partial z}(z_0)\right) x'(t) = F_{th}(t) \quad (10)$$

This means that in case of small oscillations, as for instance the thermally excited oscillations, the presence of a force gradient results in a change of effective stiffness of the system

$$k^* = k - \frac{\partial F_{ts}}{\partial z} \quad (11)$$

Since $\omega'_0 = 2\pi f'_0 = \sqrt{k^*/m}$, the cantilever resonance frequency is modified as

$$f'_0 = f_0 \sqrt{1 - \frac{1}{k} \frac{\partial F_{ts}}{\partial z}}$$

In case of small force gradient, $|\partial F_{ts}/\partial z| \ll k$, the shift in eigenfrequency $\Delta f = f'_0 - f_0$ becomes proportional to the force gradient

$$\frac{\partial F_{ts}}{\partial z} = -2k \frac{\Delta f}{f_0} \quad (12)$$

Therefore, one can determine the tip-sample force gradient by measuring the frequency shift Δf . Approaching the surface, the attractive tip-sample force causes a sudden jump-to-contact. In the quasi-static mode, the instability occurs at a distance z_{jtc} where

$$\left| \frac{\partial F_{ts}}{\partial z}(z_{jtc}) \right| > k \quad (13)$$

so that only the long range part of the interaction curve is accessible (Giessibl, 2003; Hutter & Bechhoefer, 1993). The jump-to-contact effect can be avoided by using stiff cantilevers and dynamic methods such as FM-AFM.

3. Time meets frequency, the mathematical framework

3.1 Fourier transform

Experimental data in dynamic atomic force spectroscopy frequently appear as a time series. Time series often are transformed in the frequency domain to describe their spectral content. A typical method for signal processing is the Fourier transform (FT). As a paradigmatic example, we will describe how Fourier analysis can be used to analyze the temporal trace of the cantilever thermal vibrations, detected by a standard AFM optical beam deflection system, and the kind of information possibly extracted. Finally, the limitations of this approach will be discussed.

The power spectral density (PSD) spectrum of the time signal, extending over a temporal interval sufficiently long to assure the needed spectral resolution, reveals peaked structures corresponding to the various oscillation eigenmodes of the cantilever beam (Fig. 3).

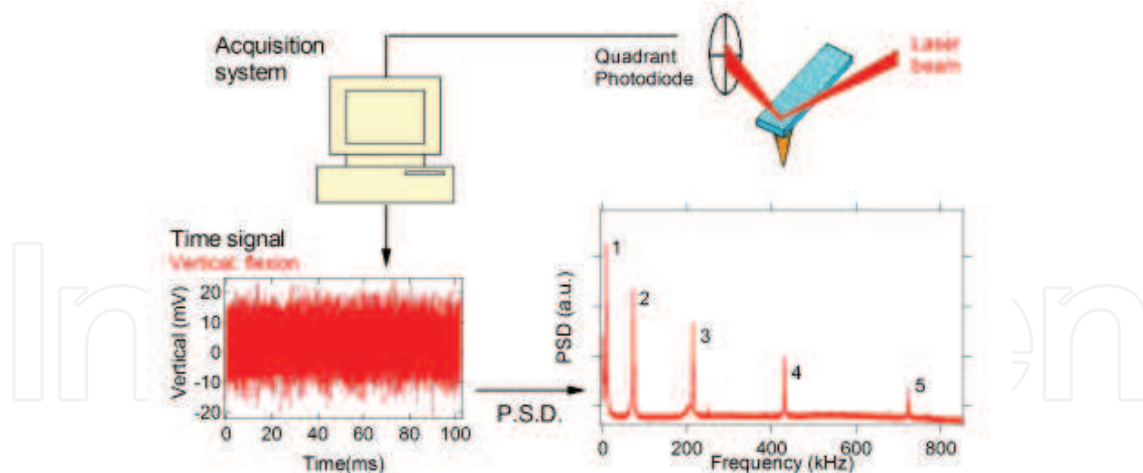


Fig. 3. Block diagram of the optical beam detection system. A typical power spectral density spectrum is shown. From (Malegori & Ferrini, 2010a).

Considering each flexural mode equivalent to a mass-spring system, the tip-sample interaction elastic constant is related to the frequency shift as $k_{ts} = -dF_{ts}/dz = 2k\Delta f/f_0$, see Eq. 12. The above relation holds if k_{ts} remains constant for the whole range of the displacements from the equilibrium position covered by the cantilever. This is usually true in the thermal regime since we are dealing with small oscillations (less than 0.2 nm) (Malegori & Ferrini, 2010a).

If this analysis is repeated at various separations from the surface, up to the jump-to-contact distance, the force gradient of the interaction dF_{ts}/dz is directly evaluated by the observed frequency shift of the PSD as a function of z .

From the same PSD, besides the force gradient, it is possible to measure the quality factor Q of the mode, that is determined by the relative width of the peaked structures corresponding to the oscillation eigenmodes of the cantilever ($\Delta\omega/\omega_0$). Q is usually dependent on the distance from the surface. Since the quality factor Q is connected to dissipation, important information on the tip-sample energy exchange can be retrieved.

With this techniques force gradients and quality factors on graphite and in air were measured by (Malegori & Ferrini, 2010a). It was found that the attractive force gradient data are well reproduced by a non-retarded van der Waals function in the form $HR/(3z^3)$ (H is the Hamaker constant and R the tip radius of curvature), up to the jump-to-contact distance which occurs at around 2 nm. In this distance range, Q is almost constant for the first and second flexural modes. This means that the interaction is conservative at distances greater than the jump-to-contact distance, the first flexural mode showing an evident decrease of the Q value just before the jump-to-contact. The dissipation mechanism related to this sharp transition is due to a local interaction of the tip apex with the surface.

In these experiments, the acquisition and storage of the photodiode time signal required tens of seconds at each tip-sample separation. This implies that the measurement at a single spatial location (one pixel of an image) may take minutes. The long measurements duration, besides the problems associated with the control of thermal drifts, is not practical for imaging purposes.

This difficulty stems from a precise characteristics of the Fourier analysis, which is devised for a stationary system i.e. the frequency spectrum is correctly correlated only with a temporally invariant physical system. For this reason, each measurement must be done in a quasi-steady state condition, requiring a long acquisition time.

As a consequence, the use of FT leaves aside many applications where the spectral content of the signal changes during the data collection. The spectral modifications are not revealed by FT, which only provides an average over the analyzed period of time and prevents correlating the frequency spectrum with the signal evolution in time. Clearly a different approach is needed to treat signals with a non-constant spectrum. In the next section, we describe a mathematical tool extremely useful to describe spectrally varying signals, the wavelet transforms.

3.2 Wavelet transforms

Perhaps one of the best ways to qualitatively appreciate the wavelet transform (WT) concept is an example. Consider a signal $f(t) = a \cos \varphi(t)$ with time varying phase $\varphi(t)$, where $\varphi(t) = \omega_0 t$ at negative times and $\varphi(t) = \omega_0 t + \alpha t^3$ at positive times (Fig. 4a). The instantaneous pulsation $\omega(t)$ is the derivative of the phase $\omega(t) = \varphi'(t)$. It is possible to see in Fig. 4b that WT analysis combines the time-domain and frequency-domain analysis so that the temporal evolution of each spectral component is determined. To confirm this, the calculated instantaneous pulsation (white line) is superposed to the signal amplitude obtained by the WT which is represented in color scale in the time-frequency plane. It is much like the concept of a musical score, where the pitch of a note (frequency) and its duration are displayed by the succession of the notes. In most cases, the wavelet analysis allows to extract accurately the instantaneous frequency information even for rapidly varying time series. To visualize the differences between the FT and WT, consider Fig. 4c. Since FT is a time invariant operator, only an average of the time-dependent spectrum is observed and the FT analysis is not able to correlate the frequency spectrum with the signal modifications in time. Instead, the wavelet transform represents the temporal trace in the time-frequency plane, providing the time dependence of both amplitude and frequency, see Fig. 4b.

To make a WT analysis, it is necessary to select an analyzing function $\Psi(t)$, called *mother wavelet*, (Mallat, 1999; Torrence & Compo, 1998). This wavelet must have zero mean and be localized in both time (unless a Fourier basis) and frequency space. An example is the Gabor wavelet, consisting of a plane wave modulated by a Gaussian

$$\Psi(t) = \frac{1}{(\sigma^2 \pi)^{1/4}} e^{\frac{t^2}{2\sigma^2} + i\eta t}$$

Here σ controls the amplitude of the Gaussian envelope, η the carrier frequency.

Dilations and translations of a mother wavelet $\Psi(t)$ generates the *daughter wavelets* as $\Psi_{s,d}(t) = \Psi(\frac{t-d}{s})$, where d is the delay and s the adimensional scale parameter. The wavelet dilations set by the scale parameter s are directly related to the frequency. The wavelet angular frequency at scale s is given by $\omega_s = \eta/s$. The associated frequency is $f_s = \omega_s/2\pi$. The wavelet translations set by the delay parameter d are obviously related to the time.

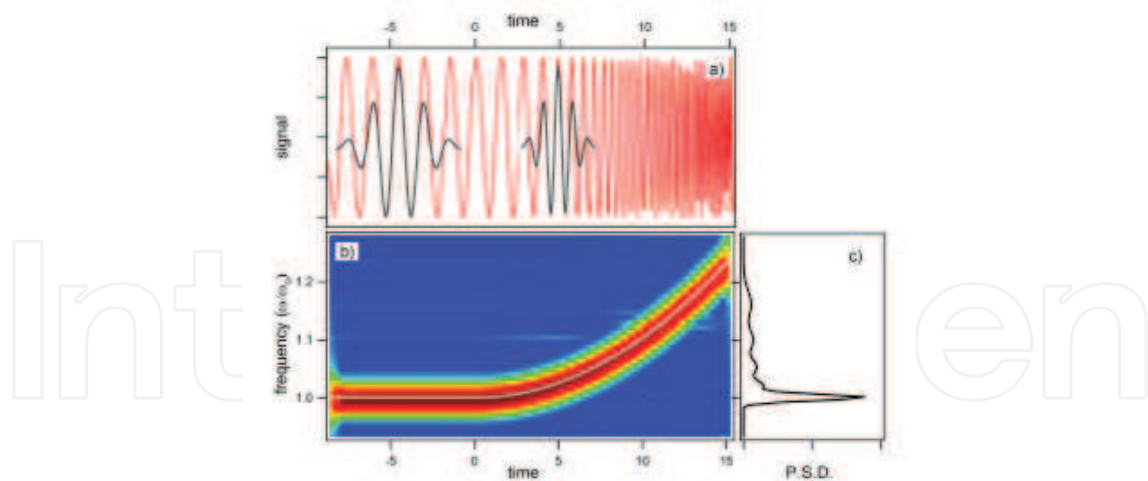


Fig. 4. Comparison between the Fourier transform and the wavelet transform analysis. a) The time signal, a cosine function for negative times and a cosine with quadratic chirp for positive times. Two daughter wavelet functions are superposed to the signal to show their localized similarity. b) Wavelet Transform of the temporal trace represented in a) showing the evolution of the frequency. The black line is the calculated instantaneous frequency. c) Fourier Transform (Power Spectral Density) of the signal represented in a). Only an average of the signal frequencies is observed. From (Malegori & Ferrini, 2010b).

The WT is defined as the convolution of the signal $f(t)$ with the daughter wavelets:

$$W(s, d) = \int_{-\infty}^{+\infty} f(t) \Psi_{s,d}^*(t) dt = \int_{-\infty}^{+\infty} f(t) \frac{1}{\sqrt{s}} \Psi^*\left(\frac{t-d}{s}\right) dt$$

The square modulus of the wavelet coefficients $|W(s, d)|^2$, called the *scalogram*, represents the local energy density of the signal as a function of scale and delay (or equivalently frequency and time). The WT compares the signal with a daughter wavelet, measuring their similarity (see waveforms superposed to the signal in Fig. 4a). The coefficients $W(s, d)$ measure the similitude between the signal and the wavelet at various scales and delays. When the frequency of a daughter wavelet is close to that of the signal at a certain time, the WT amplitude reaches the maximum at that time and frequency position.

The instantaneous frequency of the signal is evaluated by the so called *wavelets ridges*, the maxima of the normalized scalogram (Mallat, 1999). When the signal contains several spectral lines whose frequencies are sufficiently apart, the wavelet ridges separate each of these components, as shown in Fig. 5.

3.2.1 The Heisenberg box

In time-frequency analysis both time resolution and frequency resolution have to be considered. As a consequence of the Heisenberg uncertainty principle, that holds for all wavelike phenomena, they cannot be improved simultaneously: when the time resolution increases, the frequency resolution degrades and vice versa. The time-frequency accuracy of the WT is limited by the time-frequency resolution of the corresponding mother wavelet. The WT resolution is confined in a box, the Heisenberg box, one dimension denoting the time

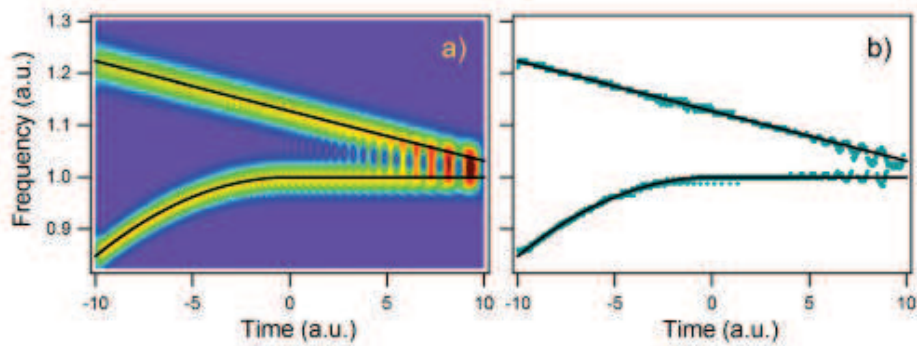


Fig. 5. a) wavelet transform of a signal that includes a linear chirp whose frequency decreases and a quadratic chirp whose frequency increases. b) The green points are the ridges calculated from the time-frequency topography. The black lines display the calculated instantaneous frequency of the linear and quadratic chirp. Note that the interference of the two spectral components destroys the ridge pattern.

resolution, the other the frequency resolution. The Heisenberg box delimits an area in the time-frequency plane over which different WT coefficients cannot be separated, providing a geometrical representation of the Heisenberg uncertainty principle. We adopt the commonly used definition of the measure of the uncertainty window Δ as the root-mean-square extension of the wavelet in the corresponding time or frequency space, (Malegori & Ferrini, 2010b),

$$\Delta_{\xi}^2 = \frac{\int_{-\infty}^{+\infty} \xi^2 |\Psi(\xi - \xi_0)|^2 d\xi}{\int_{-\infty}^{+\infty} |\Psi(\xi)|^2 d\xi}$$

where ξ_0 is a translation parameter and $\Psi(\xi)$ represents the Gabor mother wavelet, expressed either in time, $\xi = t$, or circular frequency, $\xi = \omega = 2\pi F$, $\Psi(\omega) = \text{FT}(\Psi(t))$.

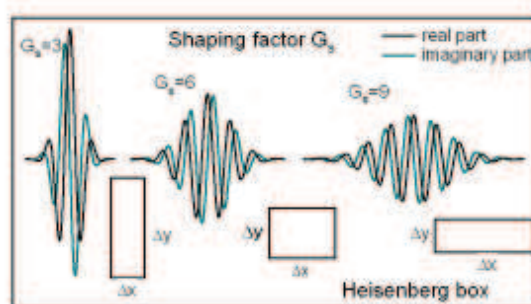


Fig. 6. Complex Gabor wavelet with different shaping factors. An increase of G_s corresponds to more oscillations. The "Heisenberg box" depicts the relationship between the time and frequency resolution, like the uncertainty principle in quantum mechanics (adapted from (Deng et al., 2005))

The time-frequency resolution of the analyzing Gabor mother wavelet, used in this work, is determined by the σ parameter. The Heisenberg box associated to the mother Gabor wavelet is given by a time resolution $\Delta_t = \sigma/\sqrt{2}$ and a frequency (or pulsation) resolution $\Delta_{\omega} = 1/(\sqrt{2}\sigma)$. When the wavelet is subject to a scale dilatation s , the corresponding resolution has

size $\Delta_{s,t} = s\Delta_t$ along time and $\Delta_{s,\omega} = \Delta_\omega/s$ along frequency. The Heisenberg box centered at time t and angular frequency $\omega = 2\pi F$ is thus defined as

$$[t - \Delta_{s,t}, t + \Delta_{s,t}] \times [\omega - \Delta_{s,\omega}, \omega + \Delta_{s,\omega}]$$

The Heisenberg box area is four times $\Delta_{s,t}\Delta_{s,\omega} = 1/2$ (time resolution \times frequency resolution) and is constant at all scales. The Gabor wavelet has the least spread in both frequency and time domain with respect to the choice of every other mother wavelet.

A single dimensionless parameter called the Gabor shaping factor $G_S = \sigma\eta$ controls the time-frequency localization properties of the Gabor mother wavelet (Deng et al., 2005). An increase of G_S means more oscillations under the wavelet envelope and a larger time spread, the frequency resolution being improved and the time resolution decreased, see Fig. 6

The resolution in time and frequency depends on s in such a way that the bandwidth-to-frequency ratio $\Delta_{s,f}/f_s$ is constant. In other words, in WT the window size changes adaptively to the frequency component by using shorter time supports to analyze higher frequency components and longer time supports to analyze lower frequency components. Therefore WT can accurately extract the instantaneous frequency from signals with wide spectral variation.

4. Wavelets meet Brownian motion: experimental results

Time-frequency analysis by wavelet transform is an effective tool to characterize the spectral content of signals rapidly varying in time. In this section we review the wavelet transform analysis applied to the thermally excited dynamic force spectroscopy to get insights into fundamental thermodynamical properties of the cantilever Brownian motion as well as giving a meaningful and intuitive representation of the cantilever dynamics in time and frequency caused by the tip-sample interaction forces.

Fig. 7 shows the time-frequency representation of the thermally excited *free* cantilever, i.e. a WT of the thermal noise of the cantilever flexural modes in air and at room temperature. The distinctive characteristic is the discontinuous appearance of the time-frequency traces, due to the discreteness and the statistical nature of the cantilever thermal excitation force F_{th} . To understand the appearance of the experimental trace and the dimensions of the observed bumps we need two concepts: the Heisenberg box and the *oscillator box*, that will be introduced in the next section.

The Heisenberg box is a visualization of the wavelet resolution (in Fig. 7 the vertical rectangles represents the Heisenberg boxes). Instead the oscillator box is related to the excitation and damping of the cantilever modes seen as damped harmonic oscillators, thus limiting the joint time-frequency response of the oscillator depending on resonant frequency and dissipation (in Fig. 7 the horizontal rectangles represents the oscillator boxes).

It is remarkable that the dimension of the bumps observed in the experimental time-frequency traces are accounted for quantitatively by the dimensions of the boxes mentioned above not only for different flexural modes, but also for contact modes and torsional modes.

Moreover, we would like to emphasize that one of the advantages of the wavelet analysis lies in the possibility to carry out measurements across the jump-to-contact transition without

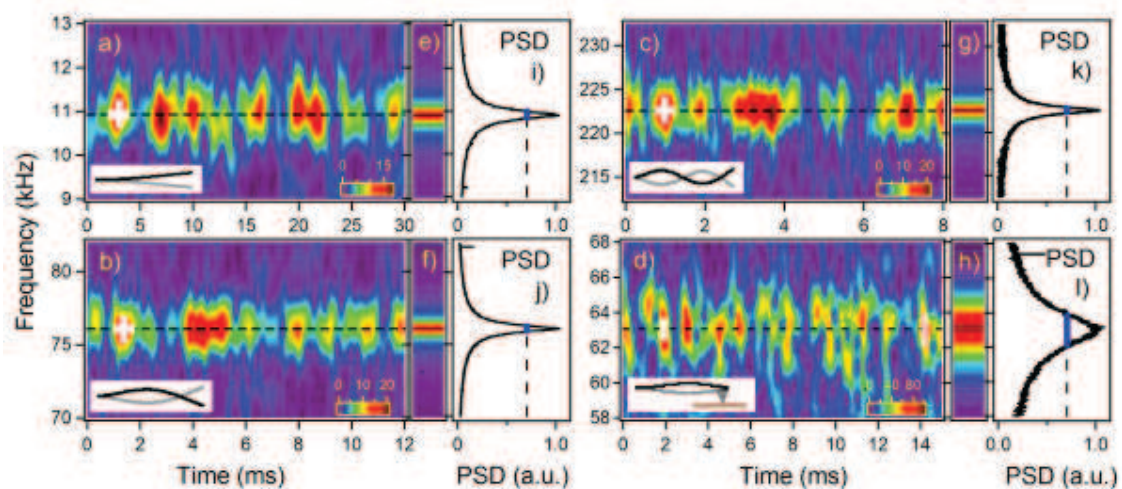


Fig. 7. a)-c) Wavelet transform of the free cantilever thermal vibrations for the three lower flexural eigenmodes. The wavelet coefficients $|W(f, t)|$ are coded in color scale. The horizontal white rectangles represent the damped oscillator boxes, the vertical rectangles the Heisenberg boxes. The dashed lines correspond to the resonant frequencies measured from the power spectral density. d) Same as a)-c) for the clamped cantilever exerting a positive load of approximately 1.1 nN on the surface. The rectangle on the left is the Heisenberg box, that on the right the damped oscillator box. i)-k) Square root of the normalized power spectral density of the free cantilever Brownian motion zoomed on the lower three resonant frequencies. The blue line is the frequency linewidth $\Delta f = f_0/Q$. The corresponding color scale plots are displayed in e)-g). l) Same as i)-k) for the clamped cantilever. The corresponding colorscale plot is displayed in h). From (Malegori & Ferrini, 2011a).

interruption (Malegori & Ferrini, 2011a), providing information on the long- and short-range adhesion surface forces. Tip-sample van der Waals interaction, adhesion forces, friction and elastic properties of the surface can be measured in few 10's of milliseconds, a time compatible with practical Dynamic Force Spectroscopy imaging.

4.1 The oscillator box

The dynamics of a free cantilever in air can be reasonably modeled as an harmonic oscillator with viscous dissipation. If no driving forces are applied, the cantilever is excited by stochastic forces whose amplitude are connected to the ambient temperature (the thermal reservoir) by the fluctuation-dissipation theorem, see Sec. 2.2. Microscopically, the external thermal force F_{th} can be thought as the action of random thermal kicks (uncorrelated impulsive forces), with a white frequency spectrum. This thermal force induces cantilever displacements from the equilibrium position, that show a marked amplitude enhancement in correspondence of the flexural eigenfrequencies.

The motion of a damped harmonic oscillator after an impulsive force excitation constitutes a simple model to describe the cantilever dynamics after a single thermal kick. When the cantilever has a thermally activated fluctuation, each flexural mode responds as a damped harmonic oscillator whose equation of motion is $\ddot{x} + \omega_0/Q\dot{x} + \omega_0^2x = 0$ where x is the oscillation amplitude (the dots denotes the derivative with respect to time), Q the quality

factor and ω_0 the resonance frequency (Albrecht et al., 1991; Demtröder, 2003). Considering for simplicity the initial conditions $x(0) = x_0$, $\dot{x}(0) = 0$ and assuming $Q \gg 1$, the solution is an exponentially decaying amplitude oscillating at the resonance frequency: $x = x_0 e^{-\omega_0 t / (2Q)} \cos(\omega_0 t)$.

The energy $E(t)$ associated to the oscillator is proportional to the maximum of \dot{x}^2 and from the above relations we see that, in case of small damping, the associated exponential energy decay time is $\tau = Q/\omega_0$. The spectral energy density of the damped oscillator ($L(\omega)$) is proportional to the square modulus of the Fourier transform of $x(t)$, $L(\omega) = |\text{FT}(x(t))|^2$. Under the assumption $Q \gg 1$, $L(\omega)$ is well approximated by a Lorentzian with a full width at maximum height of $\Delta\omega = 2\pi\Delta f = 1/\tau$.

Since the cantilever is first thermally excited and then damped to steady state by random forces that act on a much smaller time scale than its oscillation period, the characteristic response time for an isolated excitation/decay event cannot be smaller than 2τ , with an associated Lorentzian full width at half maximum of $\Delta\omega$.

From the above reasoning, it is natural to introduce the *damped oscillator box*, a geometrical representation of the extension in the time-frequency plane of the wavelet coefficients associated to a single excitation/decay event, centered at time t and frequency ω , defined as

$$[t - \tau, t + \tau] \times [\omega - \Delta\omega/2, \omega + \Delta\omega/2]$$

The damped oscillator box, contrary to the Heisenberg box, does not represent a limitation in resolution due to the wavelet choice, but a physical representation of the damped oscillator time-frequency characteristics. It is important to note that the ultimate resolution limitations imposed by the Heisenberg box associated with the analyzing wavelet could prevent the observation of the true dimensions of the damped oscillator box.

Although the free oscillation modes have very different resonant frequencies, mode shapes and relaxation times, the discrete structures near resonance have dimensions close to the respective damped oscillator boxes, within the wavelet resolution, suggesting that these structures are correlated with *single* thermal excitation events.

From the PSD shown in (Fig. 7 i,j,k), f_0 and Q are obtained from a Lorentzian fit of the resonance peaks (see Tab. 1) and the damped oscillator box dimensions are calculated. For the first, second and third free flexural eigenmodes $\tau_\gamma = 0.93, 0.38, 0.23$ ms and $\Delta\omega = 1.1, 2.7, 4.4$ kHz respectively. The Heisenberg box dimensions for the same modes are $\Delta t = 0.51, 0.18, 0.11$ ms and $\Delta\omega = 3.9, 11, 18$ kHz respectively. In this case, $\Delta t < 2\tau_\gamma$, and $\Delta\omega > \Delta\omega$. As a consequence, the temporal width of the smaller structures is about $2\tau_\gamma$, while their spectral width is determined by the wavelet frequency resolution. The temporal width of the structures is independent on the time resolution of the wavelet (provided that it is smaller than $2\tau_\gamma$), indicating that we are observing a real physical feature not related to the choice of the wavelet representation.

A different case is represented by the thermal oscillations of the surface-coupled cantilever, shown in Fig. 7d, where the tip is clamped and exerts a constant force of 1.1 nN on the surface during the measurement. In this case the tip does not oscillate and the temporal trace recorded by the optical beam deflection system is proportional to the slope at the cantilever

end. Describing this motion as a damped harmonic oscillator, we have $\tau_\gamma = 0.082$ ms and $\Delta\omega = 12$ kHz. The Heisenberg box values are $\Delta_t = 0.27$, ms and $\Delta_\omega = 7.5$ kHz. Due to the lower Q factor the spectral width is wider and the decay time smaller so that, contrary to the free cantilever case, $\Delta_t > 2\tau_\gamma$ and $\Delta_\omega < \Delta\omega$. Now the temporal width is limited by the wavelet temporal resolution while the frequency width is that of the damped oscillator. Therefore, WT describes more easily the time decay of a single thermal excitation event in high- Q environments and its frequency linewidth in low- Q environments.

We conclude observing that the discrete time-frequency small structures seen in the time-frequency representation, related to the cantilever excitation and decay to steady state by a single thermal fluctuation event, can be regarded as a visualization of the consequences of the fluctuation-dissipation theorem.

| mode | f_1 | f_2 | f_3 | f_4 | f_{c1} | f_{c2} |
|----------------|--------|-------|-------|-------|----------|----------|
| f_n (kHz) | 10.908 | 76.09 | 222.6 | 444.4 | 62.80 | 195.7 |
| Q_n | 63 | 180 | 320 | 470 | 32 | 89 |
| f_n/f_1 exp. | 1 | 6.97 | 20.4 | 40.7 | 5.75 | 17.9 |
| f_n/f_1 teo. | 1 | 6.26 | 17.5 | 34.4 | 4.38 | 14.2 |

Table 1. Free (f_1 – f_4) and clamped (f_{c1} – f_{c2}) cantilever resonant frequencies and quality factors. The measured ratio between the frequencies of the higher modes with the first one is compared with the theoretical prediction of (Butt & Jaschke, 1995).

4.2 Force spectroscopy

The wavelet analysis is applied to the force-distance curves taken with the cantilever subject to thermal fluctuations while approaching the surface. Fig. 8 shows the scalogram of a 40 ms sampling of the cantilever Brownian motion around its instantaneous equilibrium position while the piezo scanner is displaced at constant velocity to move the tip towards the surface, until it jumps to contact.

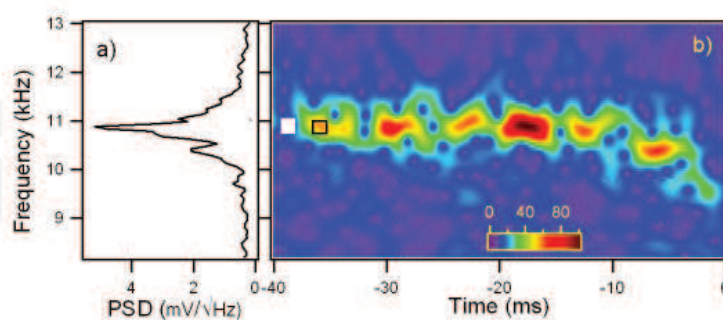


Fig. 8. a) Power Spectral Density of the Brownian motion of the first flexural mode as the tip approaches the surface at constant velocity ($9\text{nm}/40\text{ms}=225$ nm/s). b) Wavelet transform of the same temporal trace. The wavelet coefficients $|W(f, t)|$ are coded in color scale. The origin of the time axis corresponds to the instant when the jump to contact occurs. The white box on the left side is the Heisenberg box, the open box delimited by black lines is the damped oscillator box. From (Malegori & Ferrini, 2010b)

Since the cantilever is at room temperature T , its mean potential energy $1/2k\langle x^2 \rangle$ is equal to $1/2k_B T$ by the equipartition theorem. This thermal force induces cantilever

displacements from the equilibrium position, that show a marked amplitude enhancement in correspondence of the first flexural eigenfrequency. It is clear that the thermally driven eigenfrequency is affected by the tip-sample interaction forces in a small time interval prior to the jump-to-contact transition, causing a frequency decrease, as shown by the wavelet analysis in Fig. 8b. The PSD of the same temporal trace used for the WT, reported in Fig. 8a, shows a linewidth comparable to the frequency indetermination of the Heisenberg box of the WT and a structure at low frequency that is reminiscent of the interaction with the surface, when for a short time the cantilever frequency is lowered.

4.2.1 Force spectroscopy analysis

As observed previously, the instantaneous frequency is evaluated by the wavelet ridges, the local maxima points of the normalized scalogram. In order to reduce noise effects, only maxima above a threshold are considered (see the schematic representation in the inset of Fig. 9).

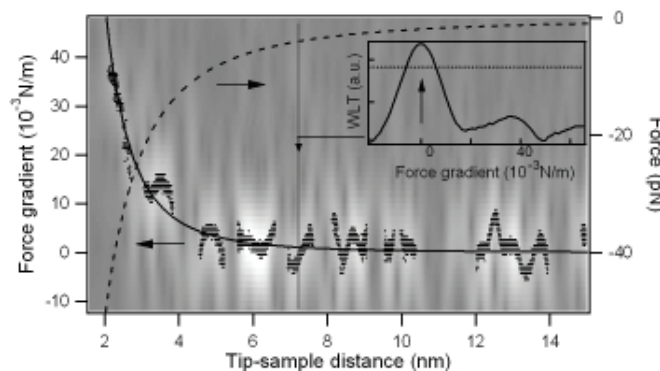


Fig. 9. Force gradient versus tip-sample distance for the first flexural mode near the jump-to-contact. The wavelet ridges provide the instantaneous frequencies within the limits of the scalogram resolution. The wavelet ridges are the local maxima of the normalized scalogram above a specified threshold, as schematically shown in the inset. The threshold is represented by a horizontal line and the maximum point is indicated by an arrow for a vertical cut of the data at constant tip-sample distance. The WT of Fig. 8 is represented in gray scale on the background together with its ridges (black points). The continuous black line is an Hamaker-like force gradient function fitted to the wavelet ridges, the dashed line the force calculated by mathematical integration. From (Malegori & Ferrini, 2010b)

The first flexural mode frequency shift near the surface (Fig. 8b) provides a complete force-distance curve using the wavelet ridges. From the instantaneous frequency shift the gradient of the tip-sample interaction forces (dF_{ts}/dz) is retrieved, using the relations previously reported. The time scale is converted into the tip-sample separation by taking into account the piezoscanner velocity and the cantilever static deflection, to obtain a complete force gradient versus distance curve (Fig. 9).

The gradient data from WT ridges are well fitted by a non-retarded van der Waals function in the form $HR/3z^{-3}$, with $HR = 1.2 \times 10^{-27}$ Jm. Using the typical values of H in graphite ($H = 0.1$ aJ), the tip radius is evaluated as $R = 12$ nm, in good agreement with the nominal radius of curvature given by the manufacturer ($R = 10$ nm). To promote this technique from

proof of principle to a measurement of the Hamaker constant with a good lateral resolution, a thorough characterization of the tip radius of curvature is needed.

The whole force curve is acquired in less than 40 ms, a time significantly shorter than that usually needed for force versus distance measurements. With an optimization of the electronics and reduction of dead times in the acquisition process, it would be possible to acquire images with the complete information on force gradients and topography compatible with 1-30 ms/pixel data acquisition times required for practical DFS imaging.

4.2.2 Contact dynamic force spectroscopy

The jump-to-contact (JTC) transition is accompanied by a high-amplitude damped oscillation of the clamped cantilever started by the impact of the tip on the surface, visible immediately after the transition. In this case the tip, attracted by the short-range adhesion forces, behaves like a nano-hammer. The wavelet transform can be carried out across the JTC transition without interruption and the oscillations induced by the JTC event are shown in the wavelet representation as a big bump in the time-frequency space (Fig. 10a). From the temporal traces we estimate that the cantilever takes approximately 10 μ s to collapse into the new state with a clamped end (Fig. 10b), a duration shorter than the system oscillation period that can be considered as instantaneous on the cantilever typical timescales. The changed boundary condition (from free to clamped cantilever end) produces a sudden variation of the flexural resonant frequencies.

In the experimental data, the time scale is converted to cantilever deflection scale taking into account the piezotube movement and the position of the surface deduced by the deflection vs distance curve (the solid-liquid interface). Negative deflection means that the beam is bent toward the sample. The load of the tip on the sample is directly calculated as $F_{load} = kx$ where k and x are the cantilever elastic constant and static deflection, respectively. In this case the loading is negative since the contact is kept by adhesion force that opposes the elastic force of the bent cantilever. The transient frequency analysis allows retrieval of the oscillator Q factor by measuring the ratio of the oscillation frequency to the frequency width of the initial high-amplitude damped oscillation. Since the Heisenberg box dimension of the analyzing wavelet is 0.27 ms \times 1.2 kHz and the frequency width is of the order of $\Delta f = 2$ kHz, the frequency width is not limited by the wavelet resolution. With a central frequency of about 60 kHz, the Q factor is obtained as $Q = f/\Delta f = 60\text{kHz}/(2\text{kHz}) = 30$. This estimate is quite consistent with the Q factor found in contact mode under static loading (Table 1), confirming that the physical oscillator (the cantilever) has the same dissipation dynamics in the various interaction-force regimes (negative and positive loading) after JTC.

The resonant frequency has an evident increase caused by the decrease in the adhesion forces due to cantilever moving towards the surface at constant velocity, a behavior reproducible in all our measurements. The frequency shift is related to the total force (adhesion plus elastic force) that decreases as the cantilever negative deflection decreases towards zero. This transient behavior could not be captured with standard or non-dynamical techniques.

It is possible to continue the contact mode WT analysis increasing the load up to higher positive values. Fig. 11 shows the ridge analysis of the entire spectroscopy curve. After the transient at negative loading described above, the cantilever passes through the zero-load

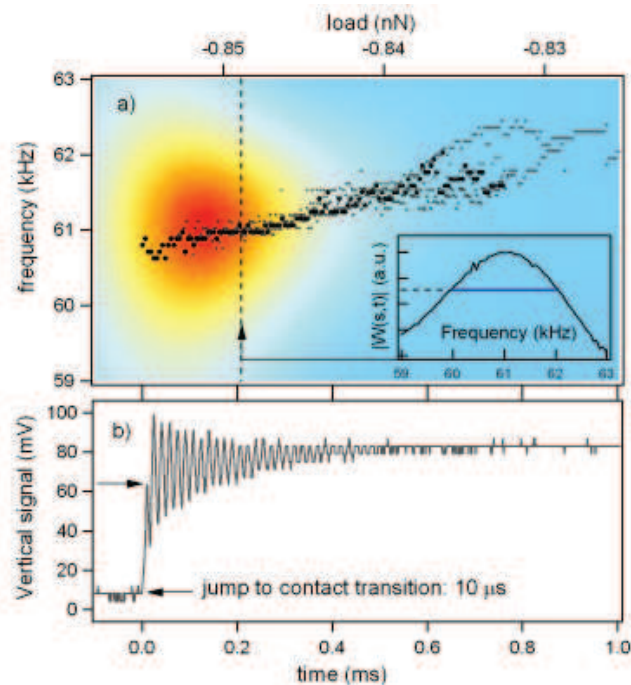


Fig. 10. a) Time-frequency representation of the cantilever evolution immediately after the jump to contact. Resonant frequency is about six times the free cantilever frequency due to changed boundary condition (clamped end). The big bump is due to the cantilever oscillations upon tip impact with the surface. The instantaneous frequency versus load is provided by the wavelet ridges analysis. Three different measurements (black, gray and light grey points) are shown to demonstrate reproducibility. In the inset: normalized wavelet coefficient $|W(f, t)|$ along the vertical dashed line. b) The temporal evolution of the clamped cantilever oscillations immediately after the jump to contact transition. It is evidenced the short time interval (approximately $10\mu\text{s}$) for the cantilever to collapse into contact. From (Malegori & Ferrini, 2011a)

neutral point, where it is not deflected, and then continues with increasing positive load on the surface. The frequency shift can be followed starting from the very beginning of the cantilever interaction with the surface and with good temporal resolution. The single measure is taken in approximately 100 ms. With an appropriate analysis, it would be possible to study in detail both the adhesion forces dynamics of the cantilever (Espinosa-Beltrán et al., 2009; Yamanaka & Nakano, 1998) and the elasticity parameters (e.g the Young's modulus) from the contact region (Hertz contact dynamics) (Dupas et al., 2001; Espinosa-Beltrán et al., 2009; Rabe et al., 1996; Vairac et al., 2003).

As a final comment to this section, we stress that the wavelet transform approach could provide quantitative information on the surface elastic properties especially when low force regimes are needed, i.e. on softer samples such as biological or polymer surfaces.

4.3 Torsional modes

The torsional modes the cantilever oscillate about its long axis and the tip moves nearly parallel to the surface, being sensitive to in-plane forces. As a consequence, the eigenfrequency of the torsional modes depends only on the lateral stiffness of the sample, serving as shear

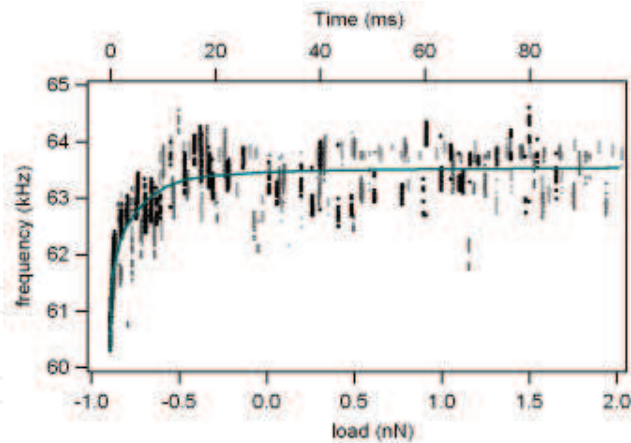


Fig. 11. Resonant frequency versus load of the first flexural contact mode, spanning the negative and positive loading regime. The instantaneous frequency versus load is provided by the wavelet ridges analysis. Three different measurements (black, gray and light gray points) are shown to demonstrate reproducibility. The continuous line is a guide to the eye. From (Malegori & Ferrini, 2011a)

stiffness sensors. An increasing shear stiffness increases the lateral spring constant and consequently the resonant frequency of the system (Drobek et al., 1999). We study the spectra of thermally excited torsional modes of the cantilever as the tip approaches a graphite surface in air (Malegori & Ferrini, 2011b). Since we are interested in exploring what happens immediately after the JTC transition, the forces that predominate in this regime are the attractive adhesion forces.

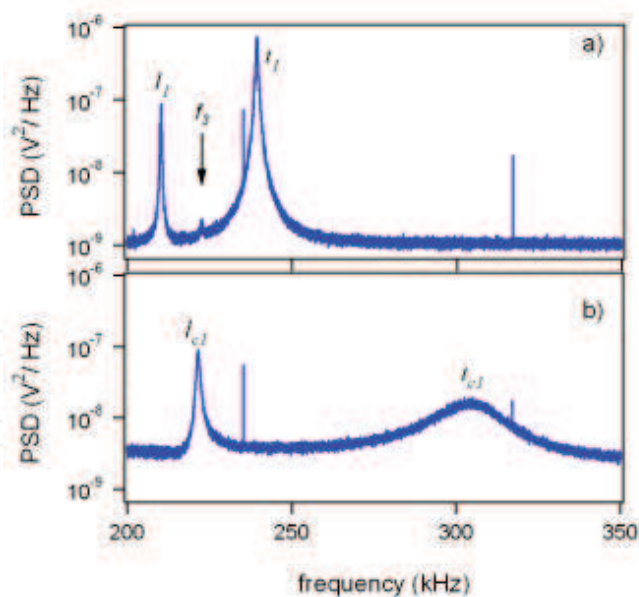


Fig. 12. a) Thermal power spectral density of the cantilever torsional fluctuations zoomed on the first torsional (t_1) and first lateral (l_1) resonance peaks. The arrow points at a small contribution from the third flexural mode (f_3) at 223 kHz. b) Same as a) but with the tip in contact with the sample at constant negative load (-0.5 nN). From (Malegori & Ferrini, 2011b).

The power density spectrum of the free cantilever first torsional modes is reported in Fig. 12a. The peak at 239.4 kHz with $Q=310$ is the first torsional mode (t_1). The mode at 210.2 kHz with $Q=590$ is the first lateral bending mode (l_1) (Espinosa-Beltrán et al., 2009). The lateral modes are cantilever in-plane flexural modes, in contrast with the usual out-of-plane flexural modes. In the spectrum is also visible a minute contribution from the third flexural mode at 222 kHz. When the tip is brought close to the sample, the capillary forces attract the tip to the HOPG surface until the JTC transition occurs (Luna et al., 1999). Due to the modified mechanical boundary conditions, the cantilever end is no longer free. A clear shift of the torsional and lateral contact mode resonances is detected under a negative static load of -0.5 nN, Fig. 12b. The first contact torsional mode resonance frequency increases to 305.2 kHz with $Q=14$; the contact lateral mode resonance frequency increases to 221.7 kHz with $Q=200$. In both cases the dissipation increases for contact modes, particularly for the first torsional eigenmode.

The torsional resonance variation of the thermally excited cantilever can be followed across the JTC transition with the wavelet transforms, as shown in Fig. 13. The JTC transition is located at time zero, separating the negative times of the free cantilever evolution, from the positive times of the clamped cantilever evolution. Note that the long-range forces and capillary phenomena that usually interfere with the oscillations of the flexural modes (Jesse et al., 2007; Malegori & Ferrini, 2010a;b; Roters & Johannsmann, 1996) do not perturb the much stiffer torsional free modes until jump-to-contact. The lateral mode frequency displays a very sharp frequency shift at JTC and remains fairly constant immediately after. Instead, the torsional contact mode shows a detectable and continuous frequency increase after JTC, caused by the tip interaction with the graphite surface.

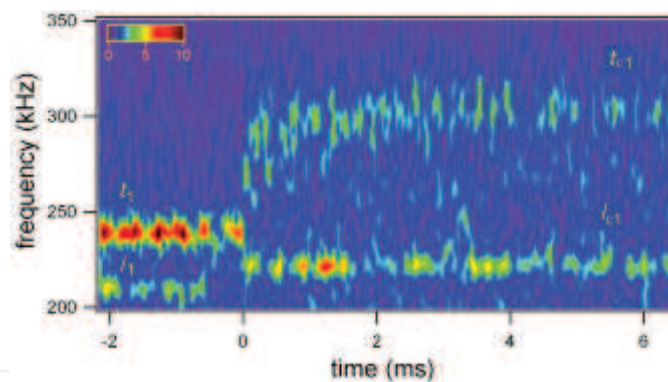


Fig. 13. Wavelet transform of the cantilever thermal torsional oscillation across the jump-to-contact transition, showing the evolution of the first free torsional mode t_1 into the contact torsional mode t_{c1} and the first free lateral mode l_1 into the contact lateral mode l_{c1} . The wavelet coefficients $|W(f, d)|$ are coded in color scale. The origin of the time axis is at the jump-to-contact onset. Both modes have an evident shift as the tip is attracted on the surface. From (Malegori & Ferrini, 2011b).

It is worth noting the different appearance of the torsional mode frequency structure before and after JTC in Fig. 13. It is evident a sudden increase of the frequency width (and a corresponding decrease of the time width) of the time-frequency trace passing through the JTC point (time zero), that can be qualitatively explained as a sudden increase in dissipation caused by the interaction with the surface. This demonstrates that there is not a smooth transition during the JTC between the free and contact oscillations.

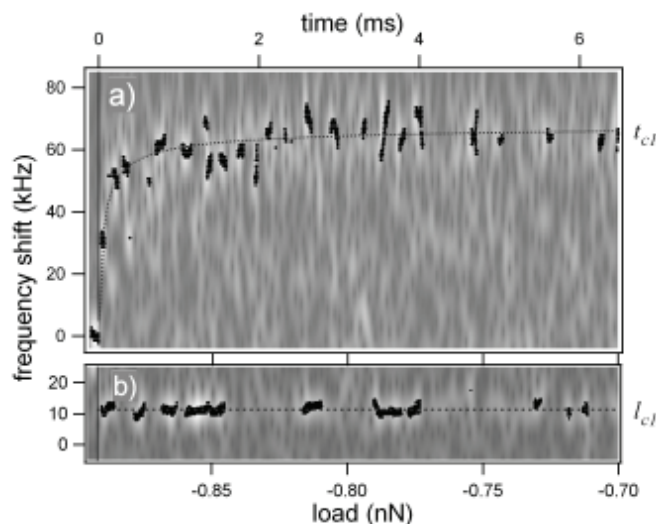


Fig. 14. a) Frequency shift with respect to the free resonant frequency of the first contact torsional mode t_{c1} versus the tip load. The ridges (black points) of the wavelet in Fig. 13, represented in gray scale on the background, provide the instantaneous frequency within the limit of the scalogram resolution. The continuous vertical line at time zero corresponds to the jump-to-contact onset. The dotted line is a guide to the eye. b) Ridges of the frequency shift with respect to the free resonant frequency of the first contact lateral mode l_{c1} versus the tip load. The dotted line is the lateral contact resonant frequency. From (Malegori & Ferrini, 2011b).

Taking into account the piezo-scanner vertical velocity, it is possible to obtain a linear relation between time and cantilever deflection, allowing calculation of the contact loading force of the tip on the surface. The frequency evolution is provided by the wavelet ridges, showing the instantaneous frequencies within the transform resolution limits in Fig. 14 as black points. Using the wavelet ridges, after JTC the time-frequency representation is transformed into a contact-interaction-force vs frequency-shift representation.

Immediately after JTC the force acting on the cantilever is negative (negative loading). In this case the tip is acted on by adhesion forces that attracts the tip towards the surface. The frequency shift of resonance frequencies with respect to the free cantilever oscillations is thus caused by the decrease in strength of adhesion forces, a transient that could not be easily captured with standard or non-dynamical techniques.

With a suitable model this technique could allow a thorough measurement of the adhesion force properties (Drobek et al., 2001; Espinosa-Beltrán et al., 2009; Yamanaka & Nakano, 1998). Analytical and numerical models describing the free cantilever-vibration as well as the contact-resonances are well known and provide quantitative evaluation when complete contact-resonance spectra are measured. The contact-resonance frequencies of the cantilever are linked to the tip-sample contact stiffness, which depends on the elastic indentation moduli of the tip and the sample and on the shape of the contact. The spatial resolution depends on the tip-sample contact radius, which is usually in the range from 10 to 100 nm. Lateral stiffness determined from the contact resonant frequencies of the first torsional vibration obtained from noise spectra have already been investigated in (Drobek et al., 2001) using quasi-static force curve cycles. The improvement provided by WT analysis is related to the time required to

detect the frequency shift vs load curve which is in the order of few ms. This acquisition time is significantly shorter than that of the quasi-static techniques and compatible with the development of real-time measurement.

To analyze a further example of the interplay between the wavelet resolution and the thermal excitation, we now consider two extreme cases: the free cantilever and the clamped cantilever with positive loading.

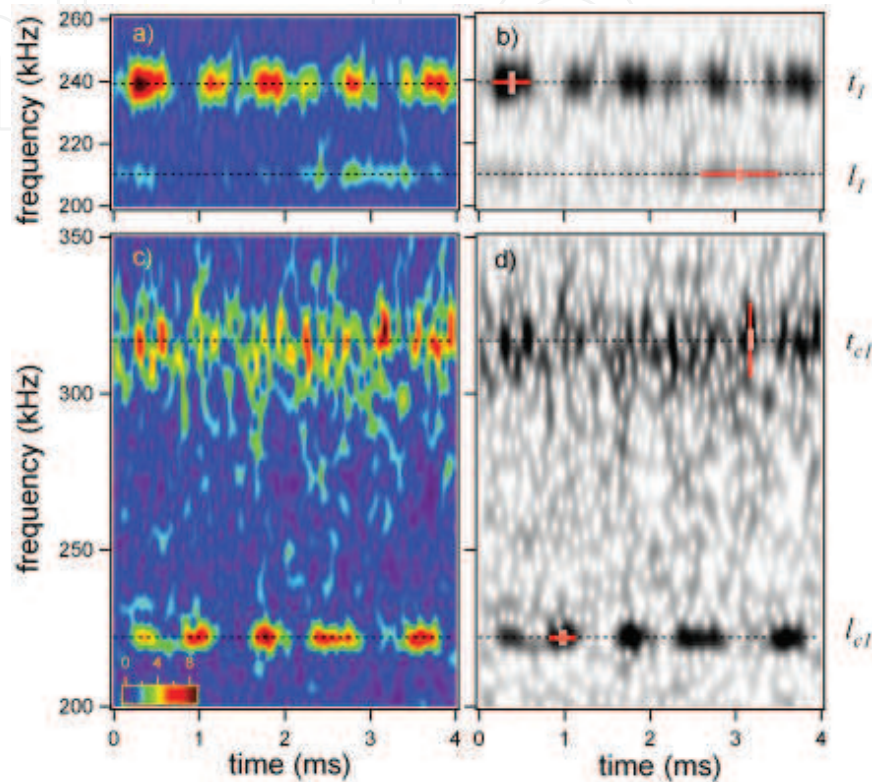


Fig. 15. a) Wavelet transform of the free cantilever thermal fluctuations of the first lateral (l_1) and first torsional (t_1) mode. The wavelet coefficients $|W(f, d)|$ are coded in color scale. The dotted lines are centered on the resonant frequencies of the modes. b) Same image as in a) but coded in saturated gray scale to appreciate the shape of the discontinuous structures. c) and d) Same as a) and b) but for the first lateral (l_{c1}) and first torsional (t_{c1}) contact mode at constant positive load of approximately 1.6 nN. In b) and d) the red rectangles with a white border represent the Heisenberg boxes. The red rectangles represent the damped oscillator boxes. From (Malegori & Ferrini, 2011b).

The wavelet transform of the free thermal oscillations of the cantilever detected by the left-right sections of the quadrant photodiode shows the time evolution of the first torsional mode and the first lateral mode (see Fig. 15a). When the Q factor of a mode is high (see Tab. 2), the corresponding frequency linewidth is small. In this case the frequency resolution of a wavelet may be not sufficient to resolve the intrinsic linewidth of the mechanical resonance. The Heisenberg box dimensions are $0.050 \text{ ms} \times 6.35 \text{ kHz}$ for the first torsional mode (t_1) and $0.057 \text{ ms} \times 5.6 \text{ kHz}$ for the first lateral mode (l_1). The damped oscillator boxes for the same modes are $0.41 \text{ ms} \times 0.77 \text{ kHz}$ (t_1) and $0.90 \text{ ms} \times 0.35 \text{ kHz}$ (l_1). Thus the frequency width of the time-frequency distribution is limited by the wavelet resolution (the frequency width of the Heisenberg box) which is much higher than the frequency width of the oscillator box (see

| mode | t_1 | t_2 | t_{c1} | t_{c2} | l_1 | l_{c1} |
|------------------------|-------|-------|----------|----------|-------|----------|
| Frequency (kHz) | 239.4 | 763.4 | 305 | 782 | 210.1 | 221.6 |
| Quality factor (Q) | 310 | 570 | 14 | 120 | 590 | 200 |
| Frequency ratio exp. | 22.0 | 70.0 | 28.0 | 71.7 | 19.3 | 20.3 |
| Frequency ratio teo. | 23.4 | 70.1 | – | – | 19.0 | – |

Table 2. Comparison between measured and calculated (Butt & Jaschke, 1995; Espinosa-Beltrán et al., 2009) free cantilever resonant frequencies. The theoretical results are expressed as ratios with respect to the first flexural frequency, $f_1 = 10.908$ kHz. The Q factors are measured from the power density spectra. t and l refers to the free torsional and lateral eigenmodes. t_c and l_c refers to the contact torsional and lateral eigenmodes. In this case the contact measurements refers to a negative load on the tip of -0.5 nN.

Fig. 15b). On the other hand, a high Q implies a long decay time associated to the oscillator energy. In this case the time associated to the damped oscillator box is larger than the temporal wavelet resolution, i.e. the time width of the oscillator box is larger than the time width of the Heisenberg box. In Fig. 15b the oscillator boxes (red) and the Heisenberg boxes (red with a white border), have been superposed on the time-frequency representation of the wavelet coefficients. In this case the Heisenberg box, i.e the wavelet resolution, limits the frequency width while the temporal extension of the structures is similar to the oscillator box time width. Such structures can be interpreted as the cantilever excitation and decay to steady state after a single thermal fluctuation event (Malegori & Ferrini, 2011a).

Fig. 15c shows the contact cantilever vibrations after JTC at a static positive load of the tip on the graphite surface of approximately 1.6 nN. The Q factor of the first torsional contact mode (t_{1c}) decreases and the oscillator box re-shapes accordingly, reducing the damping time and increasing its frequency width (Fig. 15d). We found the Q factors of the contact modes to be almost independent from the tip loading in the studied range and similar to those reported in Tab. 2 for negative loading. In this case the Heisenberg box dimensions are 0.053 ms \times 6.0 kHz for the first torsional contact mode (t_{c1}) at 316.72 kHz and 0.075 ms \times 4.2 kHz for the first lateral mode (l_{c1}) at 221.6 kHz. The damped oscillator boxes for the same modes are 0.013 ms \times 23.3 kHz (t_{c1}) and 0.28 ms \times 1.25 kHz (l_{c1}). As can be seen from the data reported above, the frequency resolution of the wavelet for the mode t_{c1} is sufficient to reconstruct the linewidth profile of the time-frequency trace, i.e. the Heisenberg box spectral width is smaller than the frequency width of the oscillator box. In contrast to the other modes, the time resolution of the wavelet does not allow to follow the temporal evolution of the single thermal excitation, because the time width of the oscillator box is smaller than the corresponding Heisenberg box dimension.

5. Conclusions

The wavelet analysis applied to dynamic AFM is especially useful in capturing the temporal evolution of the spectral response of the interacting cantilever. In this respect, the applications of wavelet analysis to the thermally driven cantilever to detect forces rapidly and continuously varying across the jump-to-contact transition must be seen as just examples and do not exhaust all the possible utilizations. Traditional AFM techniques enable the construction of the spectral response by modifying the cantilever interaction step by step. However, in this way, it is not possible to analyze transients. Instead, the wavelet analysis

allows detection of transient spectral features that are not accessible through steady state techniques. Moreover, the ability to capture the relevant spectral evolution in a time frame of tens of milliseconds enables surface chemical kinetics or surface force modification to be tracked in real time with dynamic force spectroscopy. More fundamentally, the wavelet transforms highlight the thermodynamic characteristics of the cantilever Brownian motion, enabling the tip-sample fluctuation-dissipation interactions to be investigated. In conclusion, although the results reviewed in the present work must be considered as preliminary, the proposed technique is interesting in view of its simplicity and connection with fundamental thermodynamic quantities.

6. Acknowledgments

This work has been supported by the Università Cattolica del Sacro Cuore through D.2.2 and D.3.1 grants.

7. References

- Albers, B. J., Schwendemann, T. C., Baykara, M. Z., Pilet, N., Liebmann, M., Altman, E. I. & Schwarz, U. D. (2009). Three-dimensional imaging of short-range chemical forces with picometre resolution, *Nature Nanotech.* 4: 307.
- Albrecht, T. R., Grütter, P., Horne, D. & Rugar, D. (1991). Frequency modulation detection using high-Q cantilevers for enhanced force microscope sensitivity, *J. Appl. Phys.* p. 668.
- Andreeva, N., Bassi, D., Cappa, F., Cocconcelli, P., Parmigiani, F. & Ferrini, G. (2010). Nanomechanical analysis of clostridium tyrobutyricum spores, *Micron* 41: 945.
- Binnig, G., Quate, C. C. & Gerber, C. (1986). Atomic force microscope, *Phys. Rev. Lett.* 56: 930.
- Binnig, G., Rohrer, H., Gerber, C. & Weibel, E. (1982). Surface studies by scanning tunneling microscopy, *Phys. Rev. Lett.* 49: 57.
- Braga, P. C. & Ricci, D. (2004). *Atomic force microscopy: biomedical methods and applications*, Humana Press Inc.
- Butt, H. J., Cappella, B. & Kappl, M. (2005). Force measurements with the atomic force microscope: Technique, interpretation and applications, *Surf. Sci. Reports* 59: 1.
- Butt, H.-J. & Jaschke, M. (1995). Calculation of thermal noise in atomic force microscopy, *Nanotechnology* 6: 1.
- Callen, H. B. & Greene, R. F. (1952). On a theorem of irreversible thermodynamics, *Phys. Rev.* 86: 702.
- Cappella, B. & Dietler, G. (1999). Force-distance curves by atomic force microscopy, *Surf. Sci. Reports* 34: 1.
- Cleveland, J. P., Schäffer, T. E. & Hansma, P. K. (1995). Probing oscillatory hydration potentials using thermal-mechanical noise in an atomic-force microscope, *Phys. Rev. B* 52: R8692.
- Crittenden, S., Raman, A. & Reifenberger, R. (2005). Probing attractive forces at the nanoscale using higher-harmonic dynamic force microscopy, *Phys. Rev. B* 72: 235422.
- Demtröder, W. (2003). *Laser Spectroscopy*, third edn, Springer.
- Deng, Y., Wang, C., Chai, L. & Zhang, Z. (2005). Determination of Gabor wavelet shaping factor for accurate phase retrieval with wavelet-transform, *Appl. Phys. B* 81: 1107.

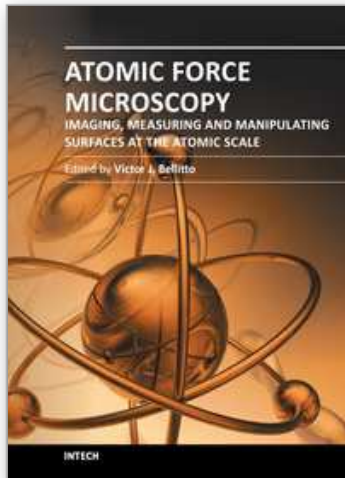
- Drobek, T., Stark, R. W., Gräber, M. & Heckl, W. M. (1999). Overtone atomic force microscopy studies of decagonal quasicrystal surfaces, *New J. Phys.* 1: 15.1.
- Drobek, T., Stark, R. W. & Heckl, W. M. (2001). Determination of shear stiffness based on thermal noise analysis in atomic force microscopy: Passive overtone microscopy, *Phys. Rev. B* 64: 045401.
- Dupas, E., Gremaud, G., Kulik, A. & Loubet, J.-L. (2001). High-frequency mechanical spectroscopy with an atomic force microscope, *Rev. Sci. Instrum.* 72: 3891.
- Espinosa-Beltrán, F. J., Geng, K., Muñoz Saldaña, J., Rabe, U., Hirsekorn, S. & Arnold, W. (2009). Simulation of vibrational resonances of stiff AFM cantilevers by finite element methods, *New J. Phys.* 11: 083034.
- Fukuma, T. (2010). Water distribution at solid/liquid interfaces visualized by frequency modulation atomic force microscopy, *Sci. Technol. Adv. Mater.* 11: 033003.
- Fukuma, T., Ueda, Y., Yoshioka, S. & Asakawa, H. (2010). Atomic-scale distribution of water molecules at the mica-water interface visualized by three-dimensional scanning force microscopy, *Phys. Rev. Lett.* 104: 016101.
- Garcia, R. (2010). *Amplitude modulation atomic force spectroscopy*, first edn, Wiley-VCH.
- Garcia, R. & Perez, R. (2002). Dynamic afm methods, *Surf. Sci. Reports* 47: 197.
- Giessibl, F. J. (2003). Advances in atomic force microscopy, *Rev. Mod. Phys.* 75: 949.
- Gillespie, D. T. (1993). Fluctuation and dissipation in brownian motion, *Am. J. Phys.* 61: 1077.
- Gillespie, D. T. (1996). The mathematics of Brownian motion and Johnson noise, *Am. J. Phys.* 64: 225.
- Gross, L., Mohn, F., Moll, N., Liljeroth, P. & Meyer, G. (2009). The chemical structure of a molecule resolved by atomic force microscopy, *Science* 325: 1110.
- Heinz, W. F., Antonik, M. D. & Hoh, J. H. (2000). Reconstructing local interaction potentials from perturbations to the thermally driven motion of an atomic force microscope cantilever, *J. Phys. Chem. B* 104: 622.
- Hölscher, H., Allers, W., Schwarz, U. D., Schwarz, A. & Wiesendanger, R. (1999). Determination of tip-sample interaction potentials by dynamic force spectroscopy, *Phys. Rev. Lett.* 83: 4780.
- Hutter, J. L. & Bechhoefer, J. (1993). Calibration of atomic-force microscope tips, *Rev. Sci. Instrum.* 64: 1868.
- Jandt, K. (2001). Atomic force microscopy of biomaterials surfaces and interfaces, *Surf. Sci.* 491: 303.
- Jena, B. P. & Hörber, J. K. H. (eds) (2002). *Atomic Force Microscopy in Cell Biology*, Academic Press.
- Jesse, S., Kalinin, S. V., Proksch, R., Baddorf, A. P. & Rodriguez, B. J. (2007). The band excitation method in scanning probe microscopy for rapid mapping of energy dissipation on the nanoscale, *Nanotechnology* 18: 435503.
- Kopniczky, J. (2003). *Nanostructures Studied by Atomic Force Microscopy*, Acta Universitatis Upsaliensis, Uppsala Sweden.
- Koralek, D. O., Heintz, W. F., Antonik, M. D., Baik, A. & Hoh, J. H. (2000). Probing deep interaction potentials with white-noise-driven atomic force microscope cantilevers, *Appl. Phys. Lett.* 76: 2952.
- Lantz, M. A., Hug, H. J., Hoffmann, R., van Schendel, P. J. A., Kappenberger, P., Martin, S., Baratoff, A. & Güntherodt, H. J. (2001). Quantitative measurement of short-range chemical bonding forces, *Science* 291: 2580.

- Luna, M., Colchero, J. & Baró, A. M. (1999). Study of water droplets and films on graphite by noncontact scanning force microscopy, *J. Phys. Chem. B* 103: 9576.
- Malegori, G. & Ferrini, G. (2010a). Tip-sample interactions on graphite studied in the thermal oscillation regime, *J. Vac. Sci. Technol. B* 28: C4B18.
- Malegori, G. & Ferrini, G. (2010b). Tip-sample interactions on graphite studied using the wavelet transform, *Beilstein J. Nanotechnol.* 1: 172.
- Malegori, G. & Ferrini, G. (2011a). Wavelet transforms to probe long- and short-range forces by thermally excited dynamic force spectroscopy, *Nanotechnology* 22: 195702.
- Malegori, G. & Ferrini, G. (2011b). Wavelet transforms to probe the torsional modes of a thermally excited cantilever across the jump-to-contact transition: Preliminary results, *e-J. Surf. Sci. Nanotech.* 9: 228.
- Mallat, S. G. (1999). *A Wavelet Tour of Signal Processing*, Academic Press.
- Martin, Y., Williams, C. C. & Wickramasinghe, H. K. (1987). Atomic force microscope-force mapping and profiling on a sub 100- scale, *J. Appl. Phys.* 61: 4723.
- Mironov, V. L. (2004). *Fundamentals of scanning probe microscopy*, The Russian Academy of Sciences, Nizhniy Novgorod Russia.
- Morita, S., Giessibl, F. J. & Wiesendanger, R. (eds) (2009). *Noncontact Atomic Force Microscopy*, Vol. II, Springer, Berlin.
- Morita, S., Wiesendanger, R. & Meyer, E. (eds) (2002). *Noncontact Atomic Force Microscopy*, Springer, Berlin.
- Palacios-Lidón, E. & Colchero, J. (2006). Quantitative analysis of tip-sample interaction in non-contact scanning force spectroscopy, *Nanotechnology* 17: 5491.
- Paolino, P. & Bellon, L. (2009). Frequency dependence of viscous and viscoelastic dissipation in coated micro-cantilevers from noise measurement, *Nanotechnology* 20: 405705.
- Rabe, U., Janser, K. & Arnold, W. (1996). Vibrations of free and surface-coupled atomic force microscope cantilevers: Theory and experiment, *Rev. Sci. Instrum.* 67: 3281.
- Radmacher, M., Fritz, M., Kacher, C. M., Cleveland, J. P. & Hansma, P. K. (1996). Measuring the viscoelastic properties of human platelets with the atomic force microscope, *Biophys. J.* 70: 556.
- Roters, A. & Johannsmann, D. (1996). Distance-dependent noise measurements in scanning force microscopy, *J. Phys.: Condens. Matter* 8: 7561.
- Sader, J. E. (1999). Calibration of rectangular atomic force microscope cantilevers, *Rev. Sci. Instrum.* 70: 3967.
- Sader, J. E. & Jarvis, S. P. (2004). Accurate formulas for interaction force and energy in frequency modulation force spectroscopy, *Appl. Phys. Lett.* 84: 1801.
- Shusteff, M., Burg, T. P. & Manalis, S. R. (2006). Measuring Boltzmann's constant with a low-cost atomic force microscope: An undergraduate experiment, *Am. J. Phys.* 74: 873.
- Sugimoto, Y., Innami, S., Abe, M., Custance, O. & Morita, S. (2007). Dynamic force spectroscopy using cantilever higher flexural modes, *Appl. Phys. Lett.* 91: 093120.
- Sugimoto, Y., Pou, P., Abe, M., Jelinek, P., Pérez, R., Morita, S. & Custance, O. (2007). Chemical identification of individual surface atoms by atomic force microscopy, *Nature* 446: 05530.
- Torrence, T. & Compo, G. P. (1998). A practical guide to wavelet analysis, *Bull. Am. Meteorological Soc.* 79: 61.

- Vairac, P., Cretin, B. & Kulik, A. J. (2003). Towards dynamical force microscopy using optical probing of thermomechanical noise, *Appl. Phys. Lett.* 83: 3824.
- Yacoot, A. & Koenders, L. (2008). Aspects of scanning force microscope probes and their effects on dimensional measurement, *J. Phys. D: Appl. Phys.* 41: 103001.
- Yamanaka, K. & Nakano, S. (1998). Quantitative elasticity evaluation by contact resonance in an atomic force microscope, *Appl. Phys. A* 66: S313.

IntechOpen

IntechOpen



Atomic Force Microscopy - Imaging, Measuring and Manipulating Surfaces at the Atomic Scale

Edited by Dr. Victor Bellitto

ISBN 978-953-51-0414-8

Hard cover, 256 pages

Publisher InTech

Published online 23, March, 2012

Published in print edition March, 2012

With the advent of the atomic force microscope (AFM) came an extremely valuable analytical resource and technique useful for the qualitative and quantitative surface analysis with sub-nanometer resolution. In addition, samples studied with an AFM do not require any special pretreatments that may alter or damage the sample and permits a three dimensional investigation of the surface. This book presents a collection of current research from scientists throughout the world that employ atomic force microscopy in their investigations. The technique has become widely accepted and used in obtaining valuable data in a wide variety of fields. It is impressive to see how, in a short time period since its development in 1986, it has proliferated and found many uses throughout manufacturing, research and development.

How to reference

In order to correctly reference this scholarly work, feel free to copy and paste the following:

Giovanna Malegori and Gabriele Ferrini (2012). Wavelet Transforms in Dynamic Atomic Force Spectroscopy, Atomic Force Microscopy - Imaging, Measuring and Manipulating Surfaces at the Atomic Scale, Dr. Victor Bellitto (Ed.), ISBN: 978-953-51-0414-8, InTech, Available from: <http://www.intechopen.com/books/atomic-force-microscopy-imaging-measuring-and-manipulating-surfaces-at-the-atomic-scale/wavelet-transforms-in-dynamic-atomic-force-spectroscopy>

INTECH
open science | open minds

InTech Europe

University Campus STeP Ri
Slavka Krautzeka 83/A
51000 Rijeka, Croatia
Phone: +385 (51) 770 447
Fax: +385 (51) 686 166
www.intechopen.com

InTech China

Unit 405, Office Block, Hotel Equatorial Shanghai
No.65, Yan An Road (West), Shanghai, 200040, China
中国上海市延安西路65号上海国际贵都大饭店办公楼405单元
Phone: +86-21-62489820
Fax: +86-21-62489821

© 2012 The Author(s). Licensee IntechOpen. This is an open access article distributed under the terms of the [Creative Commons Attribution 3.0 License](#), which permits unrestricted use, distribution, and reproduction in any medium, provided the original work is properly cited.

IntechOpen

IntechOpen